JOURNAL OF COMPUTATIONAL PHYSICS **137,** 130–154 (1997)
ARTICLE NO. CP975797

A Spectral Filtering Procedure for Eddy-Resolving Simulations with a Spectral Element Ocean Model

Julia G. Levin, Mohamed Iskandarani, and Dale B. Haidvogel

Institute of Marine and Coastal Sciences, Rutgers University, New Brunswick, New Jersey 08903-0231
E-mail: julia@imcs.rutgers.edu

Received August 26, 1996; revised June 12, 1997

The numerical simulation of turbulent oceanic flows is susceptible to the appearance of instabilities associated with the misrepresentation of nonlinear interactions among small-scale motions. Specialized filters and differencing schemes have been successfully used in the past to suppress the growth of these instabilities in finite-difference ocean models. Here, we introduce a new filtering procedure designed to control the growth of nonlinear instabilities in the spectral element solution of nonlinear oceanic flows. The new procedure involves two separate steps. First, a spectral filter is applied to the vorticity and divergence fields to damp oscillations in high-gradient regions and to restore spectral accuracy away from them. Second, the associated velocity field is computed from a set of Poisson equations, and its boundary conditions and interelement continuity are restored. This two-step strategy avoids the loss of C^0 continuity and the weakening of Dirichlet boundary conditions that can result when the filter is directly applied to the velocity field.

The behavior of the filter is investigated numerically on the canonical problem of the double-gyre wind-driven circulation in a rectangular basin using a spectral element shallow water model. The parameters of the simulation are chosen to produce mesoscale eddies. The filter is able to stabilize the simulation even at coarse resolution and to recover the "correct" statistical behavior with as few as two grid points per Rossby deformation radius. Finally, a simulation of the wind-driven circulation in the North Atlantic Ocean is performed to illustrate the effectiveness of the filter in realistic settings.

Key Words: spectral elements; global ocean modeling; spectral filters; shallow water equations.

0021-9991/97 $25.00

1. INTRODUCTION

The oceanic circulation exhibits regions of rapid property changes—e.g., western boundary currents, mesoscale eddies, and the thermocline. The representation of these features in basin-scale ocean models is often problematic because of the high computational cost involved in resolving their scales. (For example, a state-of-the-art ocean model may have an average resolution of only 15 km, whereas the length scale of mesoscale eddies can be as low as 10 km at high latitudes.) Since these features tend to be only marginally resolved on the model grid, they are a prime source of nonlinear instability through the generation of small-scale noise. This noise can be amplified through nonlinear interactions, particularly in high Reynolds number simulations.

Fronts and narrow features are not the only source of noise; independent of their presence, the nonlinear dynamics of the ocean can give rise to dynamical instabilities. These nonlinearities generate a continuous spectrum of scales that can accumulate energy at the high end of the wavenumber spectrum, which may also lead to a breakdown of the simulation. Various algorithms have been devised to avoid the growth of these instabilities in spectral and finite difference models of the ocean and atmosphere. In this article, we present a new filtering strategy designed to remove the unavoidable accumulation of small-scale noise from the spectral element shallow water model of [15]. We show the effectiveness of the new strategy by applying it to several model problems.

Spectral element methods are relative newcomers to geophysical fluid flow modeling. The current two-dimensional versions have been proposed in [17, 15] and solve the shallow water equations. Their effectiveness in the context of geophysical flows has been demonstrated in several oceanic and atmospheric applications [16, 11, 22]. Spectral element methods (SEM) achieve flexibility and efficiency in the simulation of geometrically and dynamically complex flows by dividing the computational domain into spectral elements wherein the solution is interpolated with high-order polynomials. Spectral element methods have exponential convergence rates for smooth solutions. However, if the solution develops shocks, or if small-scale features become only marginally resolved, as often happens in turbulent circumstances, the order of convergence drops and a loss of accuracy occurs. It is important to note that the loss of accuracy affects mostly the amplitude of the unresolved small scales; their phase speed is nevertheless well represented by the spectral element solution [9]. The loss of accuracy is accompanied by the appearance of Gibbs oscillations in the marginally resolved regions, i.e., unphysical and rapid oscillations that result from the truncation of a slowly convergent spectral series. These oscillations may be amplified through nonlinear interactions, which may in turn lead to a breakdown of the simulation.

The preferred solution to these potentially disastrous instabilities is to keep refining the grid in the high-gradient regions until the small-scale features become resolved. This prescription fits the spectral element philosophy nicely, but is limited in practice by the available computer resources. Other approaches to resolve the fronts or steep gradients include shock capturing schemes [9, 21], adaptive grids based on conforming and/or nonconforming spectral elements [3, 10], and hybrid

spectral elements and low-order schemes [2, 8]. These approaches tend to be expensive computationally, increase the complexity of the formulation, and are cumbersome to generalize to all situations.

A second approach consists of controlling the generation and growth of the small-scale features until they become resolvable on the model grid. Schemes built around this principle fall into two general categories. In the first category, the exponential growth in energy associated with the instabilities is eliminated by reformulating the discretized equations so as to ensure the discrete conservation of energy and enstrophy; a representative scheme of this class is the well-known Arakawa Jacobian [1]. In the second category, a highly scale-selective dissipation mechanism is introduced to remove the small-scale noise while leaving larger-scale features unaffected. Dissipation based on hyperviscosity [6], with a fourth-order operator or higher, has been successfully used to such ends in spectral and finite difference models. The application of hyperviscosity to conforming finite element methods is, however, problematic because the high-order operators require elements with higher order continuity than C^0, which makes the approach unappealing for the spectral element method.

Filters are an alternative means to achieve the goal of scale-selective dissipation, with the distinct advantage that they do not involve higher order operators. Filters based on the $\frac{2}{3}$ de-aliasing rule and Shapiro filters have been adopted in spectral and finite difference models to stem the growth of nonlinear instabilities. A new class of filters, called spectral filters, has been developed recently to cope with instabilities generated by sharp fronts and narrow features. Several spectral filters have been successfully used in conjunction with spectral methods (see [23, 7] and references therein), but their application in spectral element models has been limited for various reasons. First, most spectral element methods use relatively low spectral truncation; thus, a spectral filter may be underrepresented on the grid, and its application runs the risk of creating additional oscillations. Second, the straightforward application of a spectral filter on each element independently destroys boundary conditions and interelement continuity; these constraints are difficult to reimpose on the filtered fields without reintroducing noise. Note that a high-order filter that would preserve the C^0 constraint and the boundary conditions would be difficult to construct given the unstructured nature of a finite element grid.

Here we present a general filtering strategy that allows the use of spectral filters without destroying boundary conditions and interelement continuity in a spectral element shallow water model. The technique is based on the spectral filtering of vorticity and divergence rather than on the filtering of velocity directly. The two drawbacks of filtering are then avoided since, in a primitive variable formulation, vorticity and divergence boundary conditions are not usually enforced directly and the cross-element continuity of both fields is imposed only weakly. In our scheme, the filtered velocity is recovered by solving two Poisson problems which have the same boundary conditions as the original system of equations. The Poisson equations are solved with conjugate gradient iterations; since the filter influences only the high wavenumbers, the convergence is fast if the original velocity is used as an initial guess. The technique allows the preservation of spectral accuracy in the

smooth regions and is suitable for general domains and on nonuniform grids. In addition, it permits the design of adaptive filtering strategies.

The plan of this paper is as follows. A brief description of the shallow water spectral element model is given in Section 2. Section 3 describes the filtering procedure. In Section 4, the new procedure is tested on an eddy-resolving mid-latitude double gyre problem. It is shown that the spectral filtering technique reproduces the statistical behavior of mesoscale features and allows the recovery of the phenomenology on grids whose resolution is as low as 2 points per Rossby radius. Section 5 shows the results of the application of the filter on a global nonuniform grid used for an eddy-resolving simulation in the North Atlantic Ocean.

2. SPECTRAL ELEMENT SHALLOW WATER MODEL

The shallow water equations in the two-dimensional region Ω with boundary Γ have the form

$$\frac{\partial \mathbf{u}}{\partial t} + \mathbf{u} \cdot \nabla \mathbf{u} - \frac{\nabla \cdot [\nu(h+\zeta)\nabla \mathbf{u}]}{(h+\zeta)} = \mathscr{Q} \tag{1}$$

$$\frac{\partial \zeta}{\partial t} + \nabla \cdot [(h+\zeta)\mathbf{u}] = 0, \tag{2}$$

where

$$\mathscr{Q} = -\mathbf{f} \times \mathbf{u} - g\nabla\zeta - \gamma \mathbf{u} + \frac{\boldsymbol{\tau}}{\rho(h+\zeta)}$$

is the forcing in the momentum equation; $\mathbf{u} = (u, v)$ is the horizontal velocity vector; h is the resting depth of the fluid; ζ is the free surface elevation; $\mathbf{f}$ is the Coriolis force; g is the gravitational acceleration; γ is the bottom drag coefficient; ν is the lateral viscosity coefficient; ρ is the density of the fluid; $\boldsymbol{\tau}$ is the wind stress acting on the surface of the fluid; and, ∇ is the two-dimensional gradient operator.

The boundary conditions are Dirichlet conditions on $\mathbf{u}$ and/or ζ,

$$\mathbf{u} = \mathbf{u}^b \quad \text{on } \Gamma_D, \quad \zeta = \zeta^b \quad \text{on } \Gamma_D^\zeta, \tag{3}$$

and Neumann conditions on $\mathbf{u}$,

$$\nu \nabla \mathbf{u} \cdot \mathbf{n} = \mathbf{q} \quad \text{on } \Gamma_N. \tag{4}$$

Here, $\mathbf{n}$ is the unit normal to the boundary; $\mathbf{q}$ is the applied stress. We refer the reader to [4] for a discussion of the appropriate boundary conditions to apply for different forms of the shallow water equations.

The starting point of the spectral element model is the Galerkin formulation of the shallow water equations,

$$\int_A \frac{\partial \mathbf{u}}{\partial t}\,\phi\,dA = \int_A \left\{ \mathscr{D} - \mathbf{u}\cdot\nabla\mathbf{u} - \frac{\nu\nabla(h+\zeta)\cdot\nabla\mathbf{u}}{(h+\zeta)} \right\}\phi\,dA$$
$$- \int_A \nu\nabla\mathbf{u}\cdot\nabla\phi\,dA + \int_{\Gamma_N} \mathbf{q}\phi\,dS, \tag{5}$$

$$\int_A \frac{\partial \zeta}{\partial t}\,\phi^p\,dA = -\int_A \nabla\cdot[(h+\zeta)\mathbf{u}]\phi^p\,dA, \tag{6}$$

where ϕ and ϕ^p are the basis functions associated with the velocity and the surface elevation, respectively. They are square integrable functions whose first derivatives are also square integrable. The functions ϕ and ϕ^p vanish on Γ_D and Γ_D^ζ, respectively.

The spatial discretization proceeds by subdividing the domain Ω into a set of conforming quadrilateral isoparametric elements [18, 20]. In each element, the variables $\mathbf{u}$ and ζ are expanded as

$$\mathbf{u} = \sum_{i,j=0}^{N^u} \mathbf{u}_{ij}\phi_{ij}, \quad \zeta = \sum_{i,j=0}^{N^p} \zeta_{ij}\phi_{ij}^p, \tag{7}$$

where N^u and N^p are the number of nodes per element on the velocity and pressure Gauss–Lobatto grids, respectively; ϕ_{ij} and ϕ_{ij}^p are Legendre Cardinal functions defined on these grids. Expansions (7) are local within each element. The sole global requirement is that the interpolation be continuous across element boundaries, the so-called C^0 continuity requirement. The continuity of the normal derivative is enforced weakly only by the variational formulation. More detail on the spectral element discretization and the choice of basis functions ϕ_{ij} and ϕ_{ij}^p is given in [15].

3. FORMULATION OF THE TWO STEP FILTERING PROCEDURE

3.1. *The Vorticity and Divergence Equations*

Gibbs oscillations appear whenever a solution develops shocks or unresolvable gradients. In spectral and spectral element methods, these oscillations are symptomatic of a slowly convergent series that has lost its exponential convergence property. Spectral filters are designed to remedy this loss and to recover spectral accuracy away from the shock. Unfortunately, a straightforward application of a spectral filter in each element can and does destroy the C^0 continuity of the solution and affects the enforcement of the boundary conditions, particularly Dirichlet boundary conditions.

Our solution relies on filtering derived variables whose continuity across element boundaries is not essential. For the shallow water equations two such candidates are the vorticity, $\boldsymbol{\omega} = \nabla\times\mathbf{u}$, and divergence, $\delta = \nabla\cdot\mathbf{u}$. No boundary conditions are directly imposed on either variable, and their continuity across element boundaries is imposed only weakly. They have the further virtue that they are dynamically relevant variables that develop sharp fronts as the velocity gradients steepen (being differentiated quantities, they accumulate more noise than the velocity field). Furthermore, the velocity field associated with a given distribution of vorticity and divergence can be easily recovered via the solution of a set of Poisson equations.

Let $\mathscr{F}$ denote the filter operator, let $\tilde{\boldsymbol{\omega}} = \mathscr{F}(\boldsymbol{\omega})$ and $\tilde{\delta} = \mathscr{F}(\delta)$ be the filtered vorticity and divergence fields, and let $\tilde{\mathbf{u}}$ denote the associated velocity field. Then, the vector identity,

$$\nabla^2\tilde{\mathbf{u}} = \nabla\tilde{\delta} - \nabla \times \tilde{\boldsymbol{\omega}}, \tag{8}$$

yields the requisite equations for $\tilde{\mathbf{u}}$; the boundary conditions are the same as those of the original equations.

Note that in the context of the shallow water equations, the divergence does not vanish, and only the vertical component of the vorticity vector, $\tilde{\omega}$, is not zero. Hence, the Galerkin formulation of Eq. (8) in the two-dimensional case is

$$\begin{aligned}\int_A \nabla\tilde{u} \cdot \nabla\phi \, dA &= \int_A \mathbf{a} \cdot \nabla\phi \, dA + \int_{\Gamma_N} (\nabla\tilde{u} - \mathbf{a}) \cdot \mathbf{n}\phi \, dS,\\ \int_A \nabla\tilde{v} \cdot \nabla\phi \, dA &= \int_A \mathbf{b} \cdot \nabla\phi \, dA + \int_{\Gamma_N} (\nabla\tilde{v} - \mathbf{b}) \cdot \mathbf{n}\phi \, dS,\end{aligned} \tag{9}$$

where $\mathbf{a} = (\tilde{\delta}, -\tilde{\omega})$, $\mathbf{b} = (\tilde{\omega}, \tilde{\delta})$, and $\mathbf{n}$ is the outward unit vector. If the whole boundary of the domain consists of closed rigid walls where no-slip boundary conditions are enforced, then $\Gamma_N = \varnothing$. If free-slip boundary conditions are used, then $(\nabla\tilde{u} - \mathbf{a}) \cdot \mathbf{n} = 0$, $(\nabla\tilde{v} - \mathbf{b}) \cdot \mathbf{n} = 0$. Hence, in these special but common cases the boundary integrals in (9) vanish.

The solution of the two Poisson equations achieves two goals: the continuity of the velocity across element boundaries and the boundary conditions on the velocity are re-enforced; and the continuity of the normal derivatives at the element boundaries is reimposed weakly. Notice that the recovery step (9) is independent of the filter $\mathscr{F}$. Furthermore, the recovery procedure is based on the Laplace operator which tends to smooth steep gradients. Finally, the two Poisson equations can be solved independently.

The solution of Eqs. (9) is easily accomplished with conjugate gradient iterations using the unfiltered velocity, $\mathbf{u}$, as an initial guess. Since the filter is designed to damp the high wavenumbers, the error between the initial guess and the solution of (9) has high wavenumber components only, and the latter can be removed rapidly with a few iterations. In addition, the number of conjugate gradient iterations needed for convergence can be used as a diagnostic tool since it increases with the amount of noise in the system. Thus, it is possible to construct an adaptive filter, using the number of iterations as a criterion to adjust the strength of the filter and the frequency of its application.

The recovery procedure in spherical coordinates is given in Appendix A.

3.2. *The Spectral Filter*

The vorticity and divergence fields are filtered in each element independently by a spectral filter. A spectral filter operator, $\mathscr{F}(\omega)$, transforms the truncated spectral series

$$\omega(x) = \sum_{k=0}^{N} \omega_k L_k(x) \tag{10}$$

into the new series

$$\mathscr{F}(\omega) = \tilde{\omega}(x) = \sum_{k=0}^{N} \omega_k \sigma(k/N) L_k(x), \tag{11}$$

where L_k are the spectral functions, ω_k are the spectral coefficient, and k is the mode number. The function $\sigma(k/N)$ is the spectral filter.

The following is a brief discussion of spectral filters: the reader is referred to Vandeven [23] and Boyd [7] for further details. Vandeven [23] has shown that if

$$\sigma(0) = 1, \quad \sigma^{(m)}(0) = 0, \quad \sigma^{(m)}(1) = 0, \quad m = 1, ..., p,$$

then $|\tilde{\omega}(x) - \omega(x)|$ depends on N and the regularity of ω. If ω has p continuous derivatives, then

$$|\tilde{\omega}(x) - \omega(x)| \leq C \frac{1}{N^{p-1/2}}. \tag{12}$$

If ω has discontinuities, then

$$|\tilde{\omega}(x) - \omega(x)| \leq C \frac{1}{N^{p-1} d(x)^{p-1}}, \tag{13}$$

where $d(x)$ is the distance to the closest discontinuity and C is a constant. The parameter p is called the order of the filter. If the function is infinitely differentiable, it follows from estimate (12) that the error decreases exponentially with increasing order. If the function has a jump-discontinuity, the error depends on the distance to that discontinuity and falls off algebraically as $d(x)^{p-1}$. Thus a high-order filter is advantageous away from the discontinuity, whereas a low-order filter is more appropriate near it.

We have elected to adopt the lagged erfc-log spectral filter proposed by Boyd [7] (hereafter referred to as the Boyd–Vandeven filter). For large p, the filter asymptotes to the Vandeven and Euler filters [23], both of which are widely used for damping Gibbs oscillations and for sum-accelerations. However, compared to the latter two, the Boyd–Vandeven filter is easier to calculate and to manipulate since it has an analytic formulation which is continuous in both order, p, and argument, θ. This is a useful property for designing an optimum filter whose order increases with distance from singularities and unresolved boundary layers, particularly on nonuniform grids.

The Boyd–Vandeven filter has the form

$$\sigma_e(i/N, s) = \begin{cases} 1 & \text{if } i < s, \\ \frac{1}{2} \operatorname{erfc}\left(2\sqrt{p}\chi(\theta)(|\theta| - \tfrac{1}{2})\right), \ \theta = \dfrac{i-s}{N-s} & \text{if } s \leq i \leq N. \end{cases} \tag{14}$$

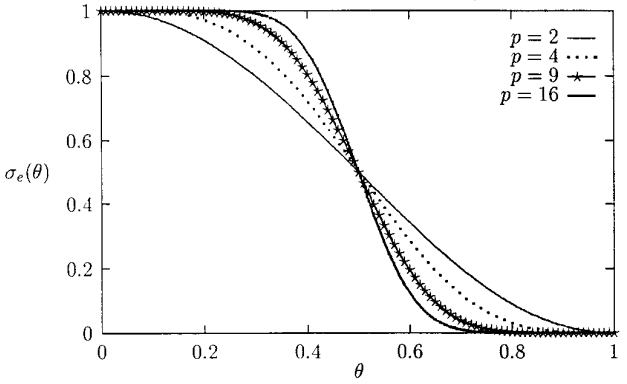

FIG. 1. Erfc-log filter $\sigma_e(\theta)$ for different values of p ($s = 0$).

where

$$\chi(\theta) = \begin{cases} 1 & \text{if } \theta = \frac{1}{2}, \\ \sqrt{-\dfrac{\log(1-4\Omega^2)}{4\Omega^2}}, \Omega(\theta) = |\theta| - \frac{1}{2} & \text{elsewhere,} \end{cases} \tag{15}$$

and s is the lagging parameter, which controls the shifting of the filter towards the high-end of the spectrum.

The Boyd–Vandeven filter obeys the Vandeven conditions and is, hence, able to recover spectral accuracy in the limit of an infinitely smooth solution. Figure 1 shows the unlagged ($s = 0$) Boyd–Vandeven filter for different values of p. The order p influences the shape of the filter. When p is large, the filter produces less dissipation of the small wavenumbers and more dissipation of the high wavenumbers. Figure 2 shows the effect of a lagged Boyd–Vandeven filter on the N^u harmon-

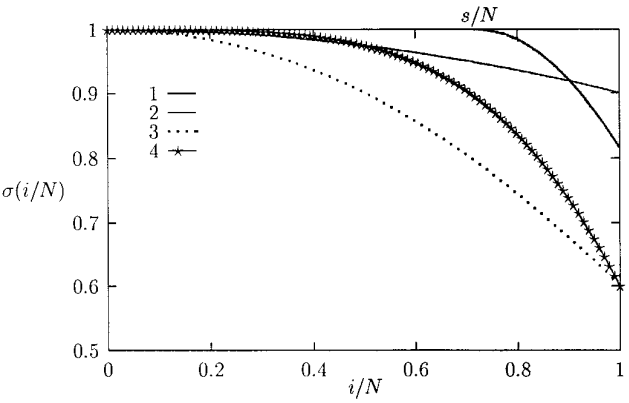

FIG. 2. Comparison of lagged Boyd–Vandeven filter with harmonic viscosity. The effect of ordinary and hyperviscosity are schematically represented in spectral space. Line 1, σ_e; line 2, ordinary viscosity with small ν; line 3, ordinary viscosity with larger ν; line 4, hyperviscosity (fourth order).

ics in a spectral expansion. The filter influences only the last several harmonics in the spectrum. In spectral space, the effect of the viscosity operator $\nu\nabla^2 u$ is analogous to a filter of the form $1 - \nu_{(2)}k^2$, where $\nu_{(2)}$ is a nondimensional viscosity parameter. The spectral filter, on the other hand, can be likened to a hyperviscosity operator, $\nu\nabla^n u$, whose representation in spectral space is analogous to the filter $1 - \nu_{(n)}k^n$. As n increases, the impact of the filter on the small wavenumbers decreases, while its effect on the large wavenumbers increases. Figure 2 shows that the viscous operator is less scale-selective than the spectral filter σ_e.

The application of the filter on a function $\omega(x)$ requires the following operations: calculation of the Legendre coefficients ω_k, application of the filter in spectral space, and the calculation of the filtered function values $\tilde{\omega}$. These three operations—Legendre transform, the application of the filter, and the inverse Legendre transform—can be incorporated in a single matrix. The filter becomes then a matrix–vector product, performed independently in each element, whose filtering matrix represents a convolution operator. This convolution operator depends on the shape of σ and on the number of Cardinal function N^u in the expansion, but is independent of the geometry of an element; thus, if uniform filtering is used the operator is the same for all elements. The operator is derived in Appendix B.

4. TEST CASE: WIND-DRIVEN CIRCULATION IN A BASIN

4.1. *Performance of the Filter on Grids with Different Resolution*

To test the performance of the filtering procedure, the spectral element shallow water model of Iskandarani *et al.* (SEOM) [15] is applied in reduced gravity mode to the canonical problem of a wind-driven, double-gyre, mid-latitude ocean in a rectangular basin [12, 14, 19]. The problem is solved in a basin of 3600×2800 km and has free-slip boundary conditions. The depth of the active layer is $h = 600$ m and the reduced gravity $g' = 0.02$ m/s^2. The Coriolis parameter in the mid-latitude β-plane approximation has the form

$$f = f_0 + \beta(y - y_0), \tag{16}$$

where $f_0 = 7.27 \times 10^{-5}$ 1/s, $\beta = 1.97 \times 10^{-11}$ 1/(ms), and $y_0 = 1400$ km.

The flow starts from rest. The circulation is forced by a steady zonal wind, which is similar to that of McCalpin and Haidvogel in [19] and has the form

$$\tau_x = \tau_0 \left\{ (1 + 4\alpha(y/L - 1/2)) \cos(2\pi y/L) - \frac{4\alpha}{2\pi} \sin(2\pi y/L) \right\}, \tag{17}$$

where $\tau_0 = -5 \times 10^{-5}$ (m/s)^2, $\alpha = 0.13$, $L = 2800$ km. The wind stress component in the meridional direction τ_y is set to zero. The wind forcing is chosen in order to produce a free jet analogous to the Gulf Stream [19]. The wind stress (17) has zero curl at the northern and southern boundaries. A bottom drag $\gamma = 1 \times 10^{-7}$ 1/s is used to balance the wind stress forcing. The viscosity $\nu = 120$ m^2/s is kept small enough to avoid dissipating the jet and the eddies. With this set of parameters, the

Rossby radius is $R = \sqrt{g'h}/f_0 = 48$ km at the central latitude, and the Munk layer thickness is $d = (\nu/\beta)^{1/3} = 18$ km.

We study the performance of the filter on grids of different resolutions. The grid of simulation A has an average resolution of 9 km, which is fine enough to resolve the scales of interest without filtering; simulation A is therefore used as the ''true'' solution. The average grid-spacing of simulations B and C are 13 and 26 km, respectively. These grids resolve the scales of interest only marginally, and filtering is needed to damp small-scale noise. Simulation D uses the same grid as simulation C but, instead of the filter, relies on a higher viscosity to stabilize the simulation. Finally, simulation E is performed on a grid with 35 km average resolution to investigate the limit of applicability of the filter on coarse grids. All grids are uniform in the meridional direction and slightly nonuniform zonally; their resolution is enhanced near the western boundary. Spectral expansions of 7×7 and 5×5 are used in all elements for the velocity and pressure grids, respectively. The time step is 1800 s for simulation E, 900 s for simulations C and D, 450 s for simulation B, and 360 s for simulation A.

Figure 2 illustrates the difference between the dissipation strategies used in simulations A–E. In simulation A dissipation is represented by line 2, which corresponds to a ''low'' laplacian viscosity. Simulations B, C, and E use a combination of low viscosity (line 2) and a lagged Boyd–Vandeven filter (line 1). In simulation D the dissipation is obtained by a higher laplacian viscosity (line 3).

Figure 3A shows a contour plot of the interface height obtained from simulation A. The simulation produces a double gyre and a turbulent mid-latitude jet. The separation point of the jet oscillates widely, and the strong meandering of the jet leads to the formation of rings. Simulations B, C, and E are computationally unstable when used without filtering. In general, the instabilities are generated either at the jet separation point or at the point where rings are pinching off. In all the experiments, we have been able to stabilize the flow by applying the vorticity-divergence filter described in Section 3. We use a filter of low order ($p = 2$) whose strength is changed by varying the lagging parameter (s in (14)) and the frequency with which the filter is applied.

Figures 3B, C shows contour plots of surface elevation obtained from simulations B and C, respectively. In simulation B, the filter is first applied at month 30, a month prior to nonlinear failure. The value of the lagging parameter is $s = 5$. The filter is applied infrequently at an average rate of once every 24 time steps. Since the filtering is moderate, the iterative solver for the Poisson problems (9) converges quickly. (The unpreconditioned conjugate gradient algorithm converges in 10–15 iterations with a convergence criterion: $|Ar|/|A| = 10^{-4}$.)

In simulation C, the filter is first applied at month 22, also a month prior to failure. The filter is lagged with $s = 4$ and is applied every six time steps. Although in this case the elliptic problem has a smaller dimension than in simulation B, the conjugate gradient method requires more iterations to converge (about 15–20 iterations in an unpreconditioned case with the same convergence criterion). This is a consequence of the stronger filtering.

Figure 3 shows realizations of the circulation at end of year 10. Given the chaotic nature of the flow, it is difficult to draw conclusions from instantaneous snap shots;

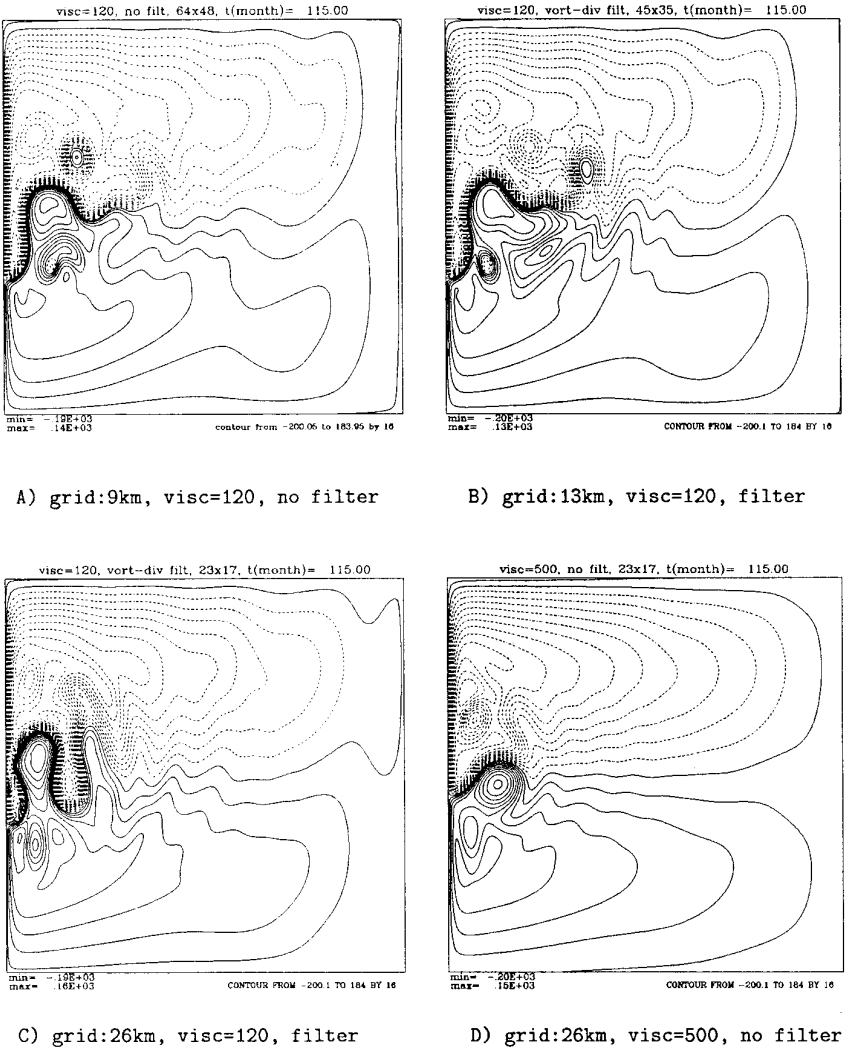

FIG. 3. Contours of instantaneous interface height. Positive contours are represented by solid lines, negative ones by dashed lines.

Fig. 3 is included as a simple illustration of the character of the flow. Examination of the time series reveals that simulations A and B are similar in the following features: the tightness of the jet, the strength of its meanders, its eddy-shedding frequency, and its eastward penetration. Simulation C exhibits the same tendencies except that its jet penetration eastward is somewhat reduced compared to cases A and B. Simulation D, on the other hand, displays weaker meanders, ring formation proceeds at a slower pace, and the jet's penetration is reduced substantially.

Although the filter is able to stabilize the simulation on grids coarser than the ones used in simulations A, B, or C, there is a resolution limit beyond which it becomes impossible to recover the mesoscale phenomenology. Figure 5a shows a

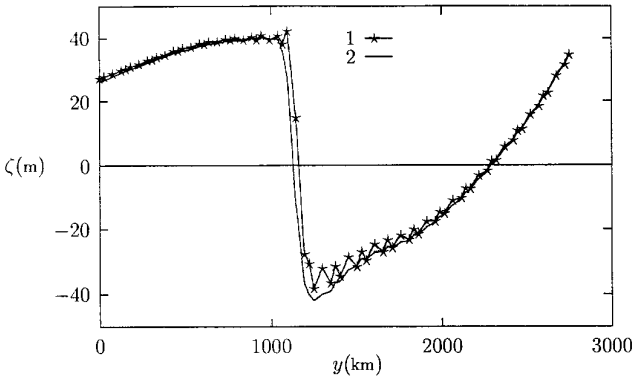

FIG. 4. Interface height along $x = 16$ km in simulation C. Line 1 shows the field at 22 months, before the filter is applied. Line 2 shows the field at 23 months, one month after filtering is started. Stars show the values at gridpoints.

snapshot from a simulation performed on the coarse grid of experiment E. The filter is the strongest here ($s = 3$) and is applied every three time steps. It does a good job of preventing the growth of the nonlinear instabilities even when the viscosity is low ($\nu = 120$ m^2/s); however, the phenomenology is distorted by the coarse resolution.

Figure 4 shows the impact of the filter in simulation C. Line 1 depicts the interface height ζ at month 22 along a line of constant x at the western boundary. No filtering has yet been applied to the field. The front is very steep and has only five grid points across it. Gibbs oscillations are present in the vicinity of the front. Line 2 shows the effect of the filtering. The vorticity-divergence filter succeeds in damping the Gibbs oscillations of the interface height but does not smear the front.

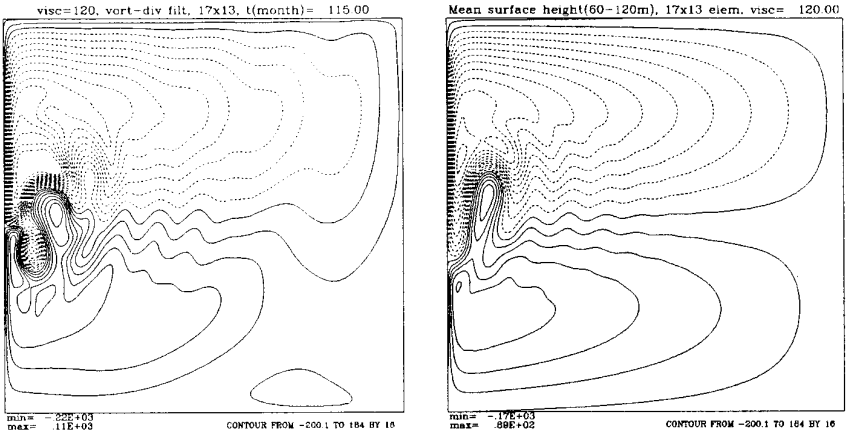

a) Contours of interface height b) Mean of interface height

FIG. 5. Results of simulation E (coarse resolution with heavy filtering).

The filtering procedure imposes a computational overhead which is mostly spent on the iterative solution of the Poisson equations. This overhead depends on the parameters of the simulation and those of the filter. The application of the filter increases the computational cost of simulation B by 20%. In simulation C, due to the increased frequency and strength of the filter, the cost of filtering becomes 50% of the total cost. The filter is, nevertheless, still cost-effective since it allows the recovery of the phenomenology on a coarser grid with a larger time step than would be necessary otherwise. For example, simulation A requires nine times more CPU time than simulation C and twice as much as simulation B.

4.2. *Statistical Analysis*

The preceding conclusions were drawn from a visual inspection of an animation of circulation A–E. In this sections we compare the different cases quantitatively based on the energy and enstrophy statistics, namely: the kinetic energy of the mean flow, the mean eddy kinetic energy, the mean kinetic energy, and the mean enstrophy, which are defined, respectively, as

$$\overline{K} = \langle \overline{h}\{\overline{u}^2 + \overline{v}^2\}/2\rangle, \tag{18}$$

$$K' = \overline{\langle h\{(u')^2 + (v')^2\}/2\rangle}, \tag{19}$$

$$K_{\text{mean}} = \overline{\langle h\{u^2 + v^2\}/2\rangle}, \tag{20}$$

$$E = \overline{\langle h(\omega')^2\rangle}, \tag{21}$$

where (u, v) is the horizontal velocity, ω is the vertical component of vorticity, h is the depth of fluid column, overbar denotes a time mean ($\overline{\xi} = (1/T) \int \xi \, dt$ for any field ξ), prime denotes a deviation from the mean ($\xi' = \xi - \overline{\xi}$), angle brackets denote the space integral: $\langle \xi \rangle = \int_A \xi \, dA$ and T is the time interval.

In all simulations, we spin up the flow from rest for the first 5 years and then take an average over the next 5 years (sampled every 3 days).

Figure 6 shows contour plots of time mean interface height for simulations A, B, C, and D. It can be seen that simulations A, B, and C produce similar fields, although the penetration of the jet is visually less on the coarser grids. Compared to the high viscosity simulation (case D); however, the penetration of the jet is considerably bigger in the filtered cases.

The superiority of filtering over high values of harmonic viscosity is demonstrated clearly in Fig. 7, which shows contour plots of the space distribution of the mean eddy kinetic energy. Most of the kinetic energy is concentrated in the western boundary layer and most of the eddy kinetic energy is near the separation point. Simulations B and C produce eddy kinetic energy distributions similar to those of reference simulation A, while the high viscosity simulation results in a noticeably different distribution: almost all of the turbulent features are dissipated.

Table I shows temporal statistics of the energy and enstrophy for the different numerical experiments. Simulations A and B are very close in all characteristics. In simulation B, the results are slightly less turbulent as indicated by the smaller eddy kinetic energy K' and by the larger energy of the mean flow $\overline{K}$. Although

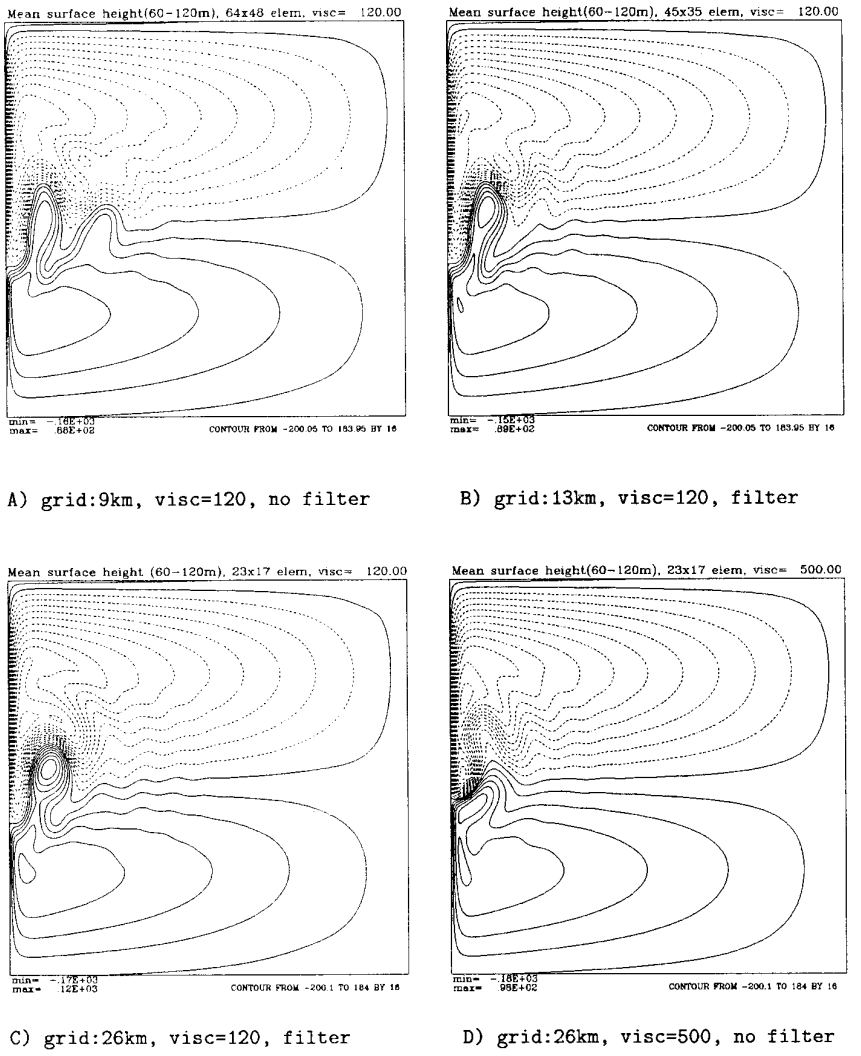

FIG. 6. Contours of mean interface height, averaged over years 5 to 10 (sampled every 3 days).

simulation C uses a stronger filter than simulation B, it displays enstrophy characteristics similar to those of simulations A and B, which shows that the filter does not distort the mesoscale features.

The situation is noticeably different in simulation D, where a large viscosity is used instead of the filter: both eddy kinetic energy and enstrophy are reduced by half. Likewise, the coarse grid of simulation E alters the statistics considerably, and the heavy filter needed to stabilize the computations leads to smaller energy and enstrophy.

There is a small increase in enstrophy between cases A and B. We attribute this to the creation of some noise when the filter is applied on grids with low spectral truncation. On such grids, the filtering function is not represented smoothly. The strong filter of simulation C decreases enstrophy but the kinetic energy is slightly

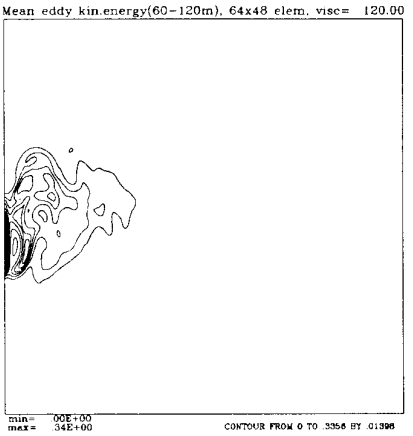

A) grid:9km, visc=120, no filter

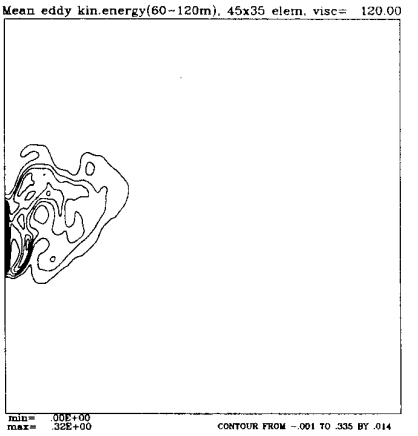

B) grid:13km, visc=120, filter

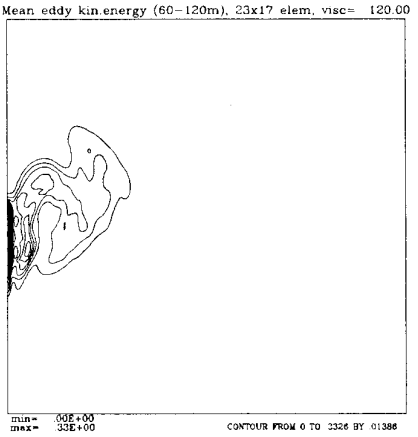

C) grid:26km, visc=120, filter

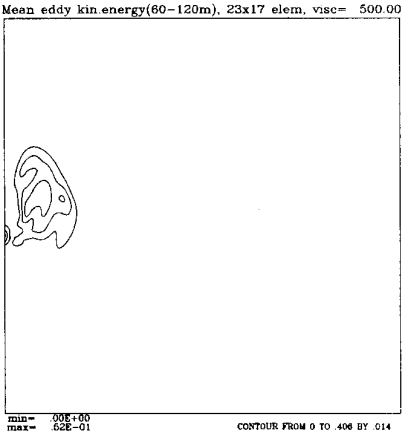

D) grid:26km, visc=500, no filter

FIG. 7. Contours of eddy kinetic energy.

TABLE I
Kinetic Energy and Enstrophy Statistics Obtained by Time Averaging during Years 5 to 10 (Sampled Every 3 Days)

	Grid	Visc	Filter	$\overline{K}(10^{13})$	$K'(10^{13})$	$K_{\text{mean}}(10^{13})$	$E(10^4)$
A	9 km	120	No	1.43	1.87	3.30	2.30
B	13 km	120	Yes	1.44	1.86	3.28	2.31
C	26 km	120	Yes	1.59	1.92	3.48	2.26
D	26 km	500	No	1.57	0.66	2.25	1.08
E	35 km	120	Yes	1.43	1.53	2.29	1.70

Note. $\overline{K}$ is kinetic energy of mean flow; K' is the eddy kinetic energy; K_{mean} is mean kinetic energy; E is mean enstrophy.

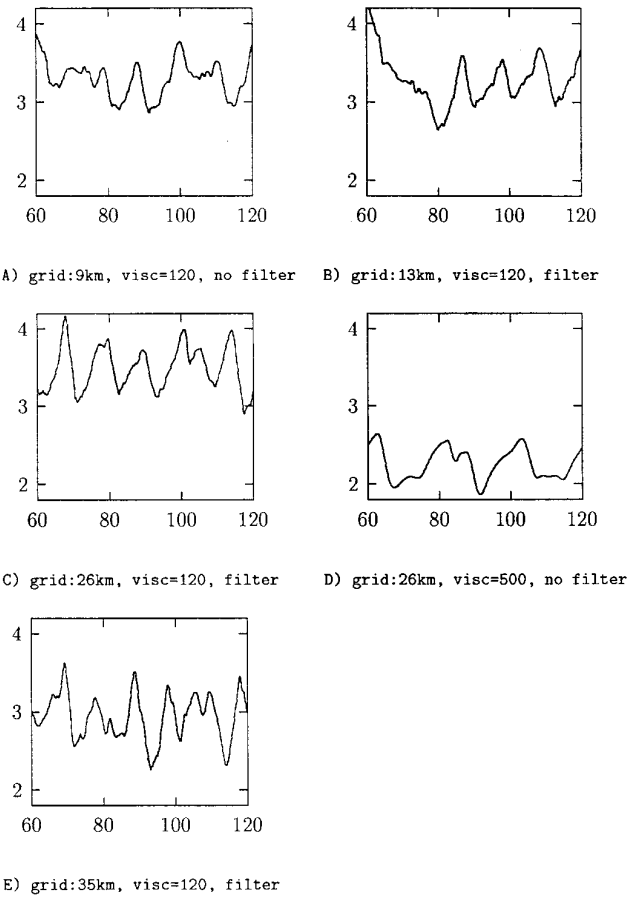

FIG. 8. Kinetic energy (shown in 10^{13} J/kg) during months 60 to 120.

larger than in simulation A. As with enstrophy and kinetic energy, filtering influences the mean height fields in a complicated way. A light filter increases the gradients of the height fields slightly, while a strong filter reduces it (see Figs. 5 and 6).

Figures 8 and 9 show the time series of kinetic energy and its discrete power spectra sampled every 3 days during years 5 to 10. The time series obtained by simulations A, B, and C (Figures 8A, B, C and 9A, B, C) have the same leading frequency of 0.0028 1/day which corresponds to the time period of 11.9 months. The leading low-frequency behavior is preserved in the filtered simulations.

On the other hand, as shown in Figs. 8D and 9D, the statistical behavior of the kinetic energy is quite different for the high viscosity simulation, case D. Roughly 25% of the kinetic energy has been dissipated. The leading fluctuation frequency is lower than in the reference time series: the strongest variability occurs on a time scale of 19.6 months, almost twice as slow as in simulation A.

Figures 8E and 9E show the results obtained on the coarsest grid, where heavy filtering is applied to stabilize the simulation. Although the energy mean is close to the mean of the reference simulation, the power spectrum is significantly affected

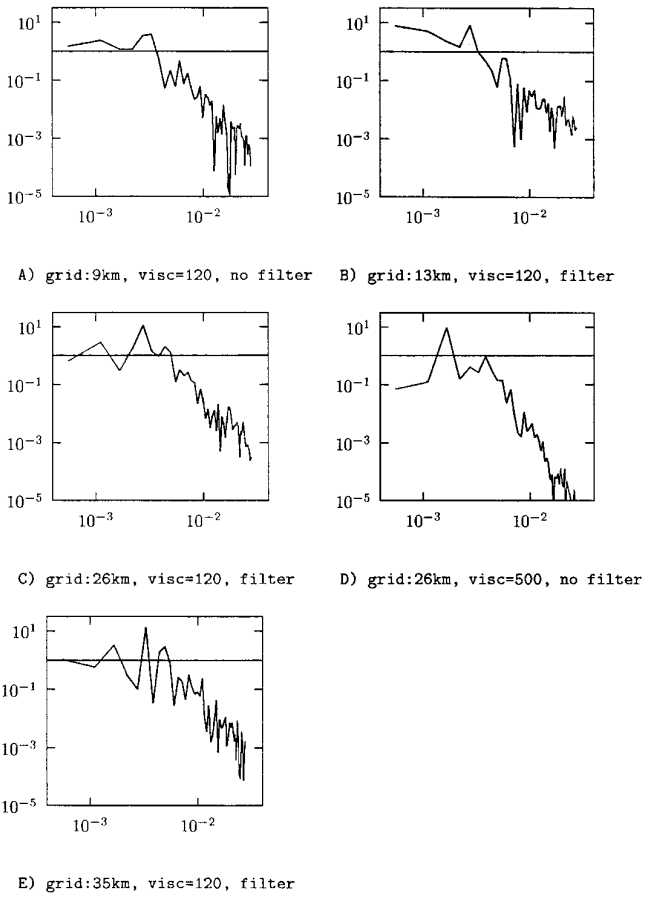

FIG. 9. Power spectrum (in log coordinates) of the kinetic energy. Abscissa shows log (frequency (1/days)).

by the filtering. In this simulation the variability occurs mostly on the time scale of 9.8 and 19.6 months.

5. AN EDDY-RESOLVING SIMULATION OF THE NORTH ATLANTIC OCEAN

In this section, we describe a simulation of the wind-driven circulation in the North Atlantic Ocean performed with SEOM [15] on a global grid. The global ocean is included in the simulation to avoid open boundary conditions. The grid resolution is enhanced in the North Atlantic Ocean (above 5°N) to resolve mesoscale eddies; elsewhere, the grid is too coarse to represent the eddies.

An effective filter for a regional simulation of this kind is more difficult to construct because the grid is nonuniform. Here the grid spacing varies from 10 km to 370 km, with an average of 21 km in the North Atlantic and 120 km in the Pacific. Figure 10 shows the global grid and, separately, the region of the North Atlantic where 75% of the grid points are located.

Viscosity is chosen to allow the production of eddies in the North Atlantic and

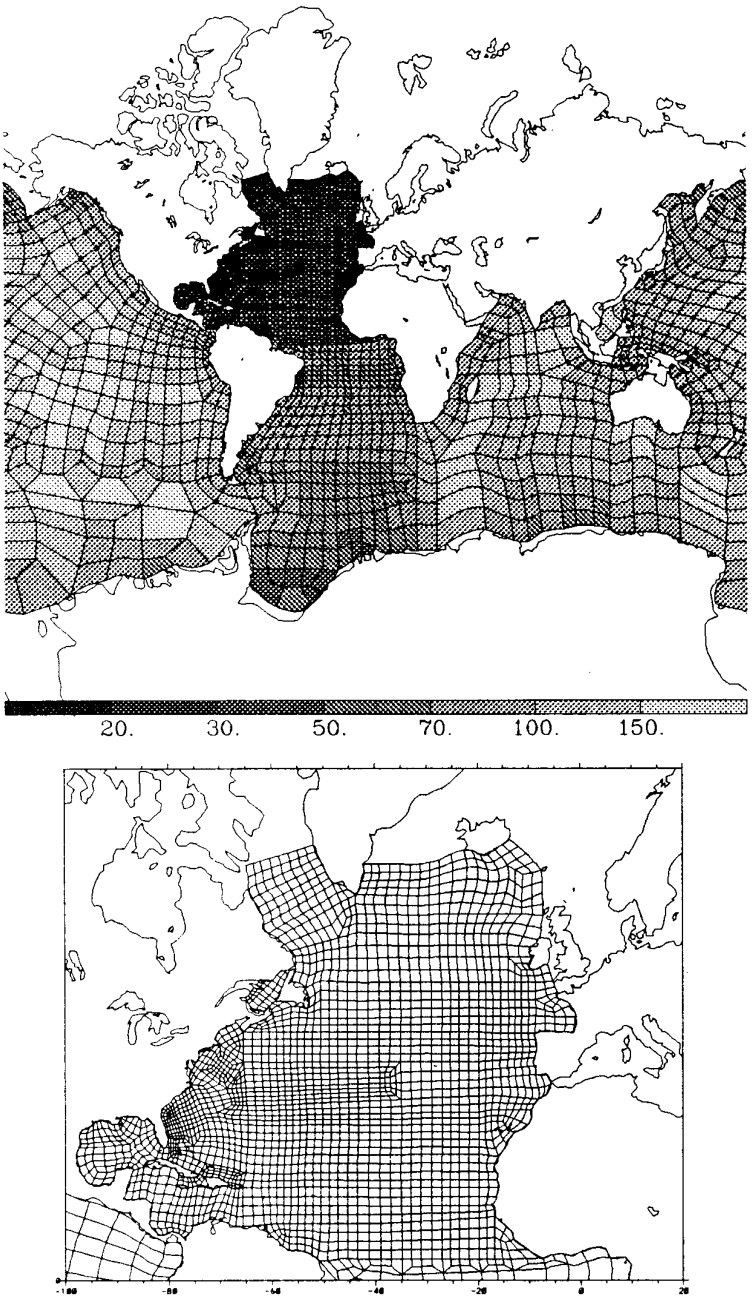

FIG. 10. Distribution of spectral elements. The mesh is refined in the North Atlantic Ocean. The grey scale code represents the average grid spacing in each element in kilometers.

to keep the flow smooth in the rest of the ocean. To achieve this, the viscosity is kept small in the North Atlantic and bigger in the rest of the ocean. Its value ranges from 55 m^2/s in the North Atlantic to 4400 m^2/s in the Pacific with an average of 100 m^2/s in the North Atlantic and 2000 m^2/s in the rest of the ocean. In each of

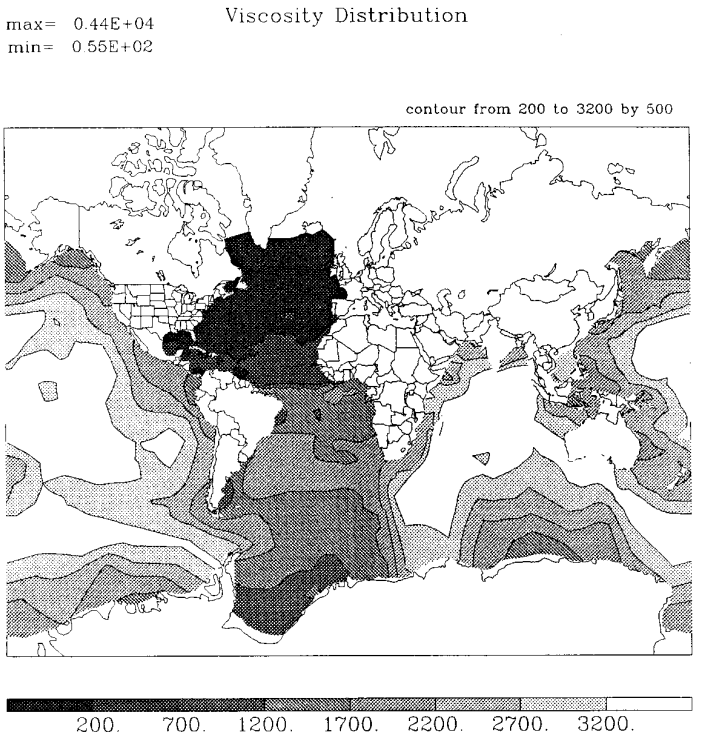

FIG. 11. Distribution of viscosity.

the regions, the viscosity is taken proportional to the maximum length of an element; such scaling produces nearly uniform grid Reynolds number with respect to the scale of the gravity wave speed. The viscosity changes gradually within an element to avoid producing oscillations on element interfaces. A contour plot of viscosity is shown in Fig. 11.

The simulation is done in reduced gravity form ($g' = 0.02$ m^2/s) with the resting layer thickness of 600 m. The only external forcing is provided by the annual mean wind stress of Hellerman and Rosenstein [13]. Integration starts from a state of rest, and no-slip boundary conditions are used. The time step is 450 s. Without filtering, the simulation fails around month 36 just as a ring is pinching off from the Gulf Stream, because the spectral element grid does not resolve all the scales of the steep gradients in the Gulf Stream region.

As shown in Section 3, an effective filter should have an order that depends on the smoothness of the fields. When the low-order vorticity-divergence filter is applied uniformly on the global grid, it may create nonphysical oscillations in regions which are already smoothly resolved on the coarse grid, whereas the same filter may be required in regions of fine resolution and narrow current features.

We use the nonuniform erfc-log filter described in Section 3. The filter order p varies from 2 in the North Atlantic to 16 in the Pacific and is scaled according to the maximum length in an element. The filter is lagged by $s = 4$ and is applied every 24 time steps. In our experiments it has been sufficient to vary the order of

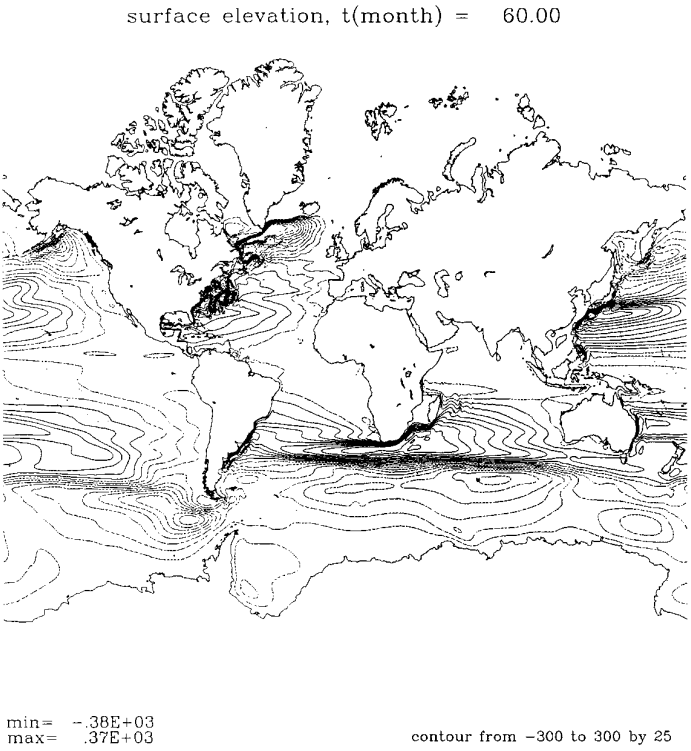

FIG. 12. Contours of surface displacement on the global grid.

the filter on an elemental basis, but a smooth change of order is also possible. The conjugate gradient method used in the recovery procedure converges reasonably fast; it requires 50–60 iterations to solve the Poisson problem with 10^6 unknowns. (The convergence criterion is the same as for the rectangular case.)

Figure 12 shows contour plots of the interface displacement at months 60, and Fig. 13 shows the North Atlantic region at months 60 and 61. Large-scale gyres and boundary currents in the Pacific and South Atlantic are roughly correct, but are weak and diffused due to the large viscosity. The filter is effective at stabilizing the simulation and at preserving the mesoscale features in the North Atlantic. The Gulf Stream, which separates correctly at Cape Hatteras, has strong meanders and ring separation. One eddy separation event is shown in Fig. 13.

A coarse, 45-km average simulation of the North Atlantic is unable to obtain Gulf Stream meandering and eddy separation. A grid of 21-km average has about 2 points per Rossby radius of deformation which is enough in the filtered model to reproduce the phenomenology. With the help of the filter, we have been able to obtain the dynamics on scales which would be dissipated had a high viscosity been used to stabilize the simulation.

6. CONCLUSION AND DISCUSSION

In this article, we have presented a filtering strategy to damp small-scale noise from spectral element computations. The strategy relies on filtering derived fields

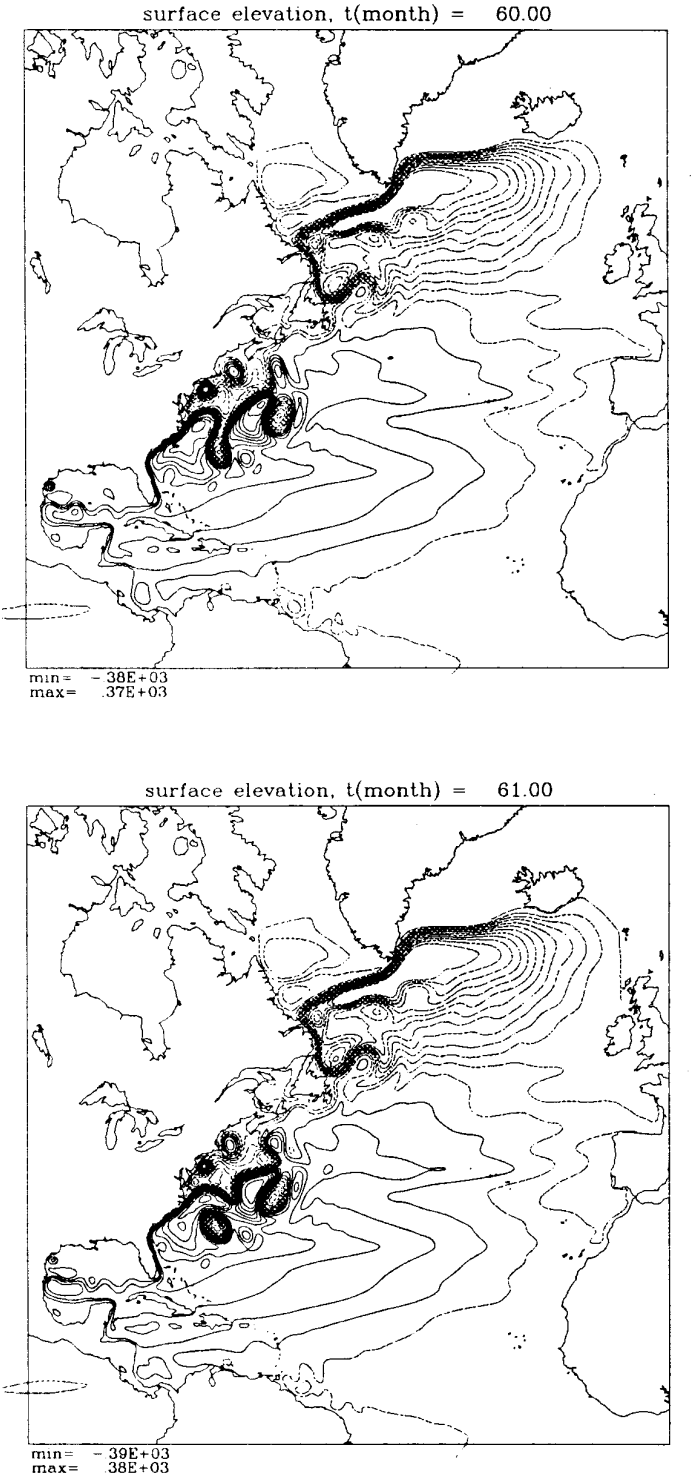

FIG. 13. Contours of surface displacement in the North Atlantic Ocean.

such as the vorticity and divergence to remove the small scales, and on the solution of Poisson equations to reimpose boundary conditions and interelement continuity of the corresponding velocity field. We remark that the height field is not filtered in our scheme, and thus, conservation of mass is preserved. The spectral Boyd–Vandeven filter provides the scale-selective mechanism needed to damp the small scales effectively while leaving the larger scales unaffected. Its scale-selection properties are superior to those of harmonic viscosity; furthermore, it does not put an additional stability restriction on the time-step and can be easily implemented in general domains.

The performance of the filter has been investigated numerically on several oceanic problems. We have performed a series of experiments on grids of different resolution to test the convergence of the filtered simulations to a reference, unfiltered, and high-resolution simulation. The filtering is very efficient at damping Gibbs oscillations and at stemming their nonlinear growth, so that the filter need not be applied too frequently. These experiments indicate that the present filtering strategy allows a spectral element shallow water model to represent accurately the rapidly varying boundary currents and mesoscale eddies on grids with resolution as low as two points per Rossby radius. We have also illustrated the application of the filter strategy in realistic oceanic settings and have shown the results of an eddy-resolving simulation in the North Atlantic Ocean, where the mesoscales are resolved only marginally. The filtering is formulated in spherical geometry and applied nonuniformly on a global, highly unstructured grid.

The two-step filtering strategy proposed herein is mostly, if not entirely, meant for spectral element or multidomain spectral methods, which require some sort of global operation to be performed on the dependent variables to reimpose global constraints after filtering is applied independently in each element or subdomain. The Poisson equation (8) is one instance of such a global operation; other ''globalization'' procedures can be devised. For example, Taylor's global operation [22] consists of averaging the solution at inter-element boundaries to reimpose the C^0 continuity constraint. Although the method works well in his spherically periodic test cases, it does not perform as well in our tests where it shows a propensity to reintroduce Gibbs oscillations near element boundaries, particularly those coincident with domain boundaries.

For purely spectral methods, the two-step procedure can be avoided altogether. Since there is no interelement continuity to worry about, the only concern is the preservation of boundary conditions. Boyd (private communication) has recently proposed a clever ''basis recombination'' for this purpose. Briefly, the solution is reexpanded in a new basis where the low-wavenumber coefficients enforce the boundary conditions (Dirichlet or Neumann), and the high-wavenumber polynomials vanish at the edges. Filtering the high-wavenumbers then leaves the boundary conditions unaffected.

The main liability in the vorticity-divergence filter is the cost incurred in solving the Poisson equations during the recovery step. Our tests have shown that this cost is low to moderate provided the filter is not removing a lot of energy from the small scales. Increased consumption of CPU by the filter is indicative of excessive small scales and points to the need for enhanced grid resolution. Nonetheless, in

all cases discussed here, the saving in CPU possible on the coarser grids more than compensates for the overhead of the elliptic solver.

The present article is just one step in formulating a full filtering strategy. The algorithm outlined here lacks procedures to automatically select the optimal parameters for the filter, i.e., its order, its lag, and its frequency of application. The values we have used in our simulations were determined experimentally. Furthermore, we have adopted the number of CG iterations as an indirect and cheap (but remarkably adequate) measure for the level of noise in our solution, and we have based our adaptive filtering strategy on it. Ideally, one would like to interrogate the solution periodically to determine when and where to apply the filter. The decision would be based on estimates of the smoothness of the solution, and/or the amount of energy contained in the smallest scales resolved by the grid. Optimal filter parameters would then be calculated based on the distance from and strength of the small-scale instabilities. The error/smoothness analysis and the parameter selection are complicated issues that merit a separate study. Finally, we would like to point out that vorticity-divergence formulation has a natural extension to the three-dimensional case.

APPENDIX A: SPHERICAL GEOMETRY

If the equations are solved in a spherical geometry, the recovery equations have to be modified. The analogues of vorticity and divergence are now defined as

$$\delta = \frac{u_\lambda}{a \cos\theta} + \frac{v_\theta}{a}, \tag{22}$$

$$\omega = \frac{v_\lambda}{a \cos\theta} - \frac{u_\theta}{a}, \tag{23}$$

where (λ, θ) are the longitudinal and latitudinal coordinates and a is the radius of the sphere. The recovery equations are then the two scalar equations,

$$\nabla^2 \tilde{u} = \nabla \cdot \mathbf{a}, \tag{24}$$

$$\nabla^2 \tilde{v} = \nabla \cdot \mathbf{b}, \tag{25}$$

where ∇^2 and ∇ are the spherical two-dimensional Laplace and divergence operators, respectively, and $\mathbf{a} = (\tilde{\delta}, -\tilde{\omega})$, $\mathbf{b} = (\tilde{\omega}, \tilde{\delta})$. The Galerkin formulation is given by Eq. (9).

APPENDIX B: FILTERING TRANSFORMATION

The $(N + 1)$ Legendre coefficients ω_k of Eq. (10) are given by [5]

$$\omega_k = \frac{\int_{-1}^{1} \omega(x) L_k(x)\, \mathrm{d}x}{\gamma_k}, \quad \gamma_k = \int_{-1}^{1} L_{k^2}(x)\, \mathrm{d}x. \tag{26}$$

Using Gauss–Lobatto quadrature to evaluate the integral in the numerator of ω_k (γ_k is known analytically), the Legendre coefficients can be approximated with

$$\omega_k = \frac{1}{\gamma_k} \sum_{l=0}^{N} \omega(x_l) L_k(x_l) \rho_l, \tag{27}$$

where the x_l and ρ_l are the $(N + 1)$ Gauss–Lobatto roots and their corresponding quadrature weights, respectively. Note that if the function ω is a polynomial of degree N, then the quadrature formula will be exact for all the Legendre coefficients except the highest one.

The filtered function $\tilde{\omega}$ can now be computed on the Gauss–Lobatto point x_i with the help of Eqs. (27) and (11):

$$\tilde{\omega}(x_i) = \sum_{k=0}^{N} \frac{1}{\gamma_k} \sum_{l=0}^{N} \omega(x_l) L_k(x_l) \rho_l \sigma_k L_k(x_i). \tag{28}$$

The above formula can be cast in the matrix–vector product form:

$$\tilde{\omega}(x_i) = \sum_{l=0}^{N} A_{il} \omega(x_l), \quad \text{where } A_{il} = \sum_{k=0}^{N} \frac{1}{\gamma_k} \rho_l \sigma_k L_k(x_l) L_k(x_i). \tag{29}$$

The matrix A_{il} lumps the forward and backward Legendre transforms and the filter application into a single operation.

The two-dimensional filter is calculated by tensor–product application of the one-dimensional formula.

ACKNOWLEDGMENTS

We thank John P. Boyd for his helpful comments and for providing us with the erfc-log filter and Mark Taylor for paving the way for its use with the spectral element method. Development and application of the spectral element ocean model is supported by grants from the Office of Naval Research (N00014-93-0197 to Rutgers University and N00014-95-1-0266 to MIT).

REFERENCES

1. A. Arakawa and V. R. Lamb, *Computational Design of the Basic Dynamical Processing of the UCLS general circulation model,* Vol. 17 (Academic Press, New York, 1977), p. 174.
2. C. Bernardi and Y. Maday, Coupling finite element and spectral methods: First results, *Math. Comput.* **54**(189), 21 (1990).
3. C. Bernardi, Y. Maday, and A. Patera, A new nonconforming approach to domain decomposition: The Mortar element method, in *Nonlinear Partial Differential Equations and Their Applications,* edited by H. Brezis and J. L. Lions (Pitman & Wiley, New York, 1992).
4. C. Bernardi and O. Pironneau, On the shallow water equations at low Reynolds numbers. *Commun. Partial Differential Equations* **16**(1), 59 (1991).
5. J. P. Boyd, *Chebyshev and Fourier Spectral Methods* (Springer-Verlag, New York/Berlin, 1989).
6. J. P. Boyd, Hyperviscous shock layers and diffusion zones: Monotonicity, spectral viscosity, and pseudospectral methods for very high order differential equations, *J. Sci. Comput.* **9**(1), 81 (1994).

7. J. P. Boyd, The Erfc-Log filter and the asymptotics of the Euler and Vandeven sum accelerations, *Houston J. Math.,* in press.
8. W. Cai, H. C. Lee, and H.-S. Oh, Coupling of spectral methods and the *p*-version of the finite element method for elliptic boundary value problems containing singularities, *J. Comput. Phys.* **108,** 314 (1993).
9. J. Giannakouros and G. E. Karniadakis, A spectral element-FCT method for the compressible Euler equations, *J. Comput. Phys.* **115,** 65 (1994).
10. H. Guillard, J. M. Malé, and R. Peyret, Adaptive spectral methods with application to mixing layer computations. *J. Comput. Phys.* **102,** 114 (1992).
11. D. B. Haidvogel, E. Curchitser, M. Iskandarani, R. Hughes, and M. Taylor, Global modeling of the ocean and atmosphere using the spectral element method, *Ocean-Atmos.,* in press.
12. D. B. Haidvogel, J. C. McWilliams, and P. R. Gent, Boundary current separation in a quasigeostrophic, eddy-resolving ocean circulation model, *J. Phys. Oceanogr.* **22,** 882 (1992).
13. S. Hellerman and M. Rosenstein, Normal monthly wind stress over the world ocean with error estimates, *J. Phys. Oceanogr.* **13,** 1093 (1983).
14. W. R. Holland, The role of mesoscale eddies in the general circulation of the ocean—Numerical experiments using a wind-driven quazi-geostrophic model, *J. Phys. Oceanogr.* **8,** 363 (1978).
15. M. Iskandarani, D. B. Haidvogel, and J. P. Boyd, A staggered spectral element model with application to the oceanic shallow water equations, *Int. J. Numer. Methods Fluids* **20,** 393 (1995).
16. H. Ma, The equatorial basin response to a rossby wave packet: The effects of nonlinear mechanism, *J. Marine Res.* **50,** 567 (1992).
17. H. Ma, A spectral element basin model for the shallow water equations, *J. Comput. Phys.* **109,** 133 (1993).
18. Y. Maday and A. T. Patera, Spectral element methods for the incompressible Navier–Stokes equations, in *State of the Art Surveys in Computational Mechanics,* edited by A. K. Noor (ASME, New York, 1988), p. 71.
19. J. D. McCalpin and D. B. Haidvogel, Phenomenology of the low-frequency variability in a reduced-gravity, quasigeostrophic double-gyre model, *J. Phys. Oceanogr.* **26**(5), 739 (1996).
20. A. T. Patera, A spectral element method for fluid dynamics: Laminar flow in a channel expansion, *J. Comput. Phys.* **54,** 468 (1984).
21. D. Sidilkover and G. E. Karniadakis, Non-oscillatory spectral element Chebyshev method for shock wave calculations, *J. Comput. Phys.* **107,** 10 (1993).
22. M. Taylor, J. Tribbia, and M. Iskandarani, The spectral element method for the shallow water equations on the sphere, *J. Comput. Phys.* to appear.
23. H. Vandeven. Family of spectral filters for discontinuous problems. *J. Sci. Comput.* **6**(2), 159 (1991).